

FULL PAPER

Open Access



Source model for the M_w 6.0 earthquake in Jiashi, China on 19 January 2020 from Sentinel-1A InSAR data

Pengfei Yu^{1,2} , Xuejun Qiao^{2*} , Wei Xiong², Wei Chen², Zhaosheng Nie², Dijin Wang², Zhige Jia² and Jie Li³

Abstract

On January 19, 2020, an M_w 6.0 earthquake occurred in Jiashi, Xinjiang Uygur Autonomous Region of China. The epicenter was located at the basin-mountain boundary between the southern Tian Shan and the Tarim Basin. Interferometric Synthetic Aperture Radar (InSAR) is used to obtain the coseismic deformation field from both ascending and descending Sentinel-1A satellite images of the European Space Agency. The results showed that the coseismic deformation is distributed between the Kalping fault and the Ozgertaou fault. The earthquake produced significant deformation over an area of approximately 40 km by 30 km. The maximum and minimal displacements along the line of sight (LOS) are 5.3 cm and -4.2 cm for the ascending interferogram and are 7.2 cm and -3.0 cm for the descending interferogram, respectively. The fault geometry from the Multi peak Particle Swarm Optimization computation indicates that the seismogenic fault is a shallow low-dipping planar fault that is 4.58 km depth underground. The finite slip model inverted by the Steepest Descent Method implies that the rupture is dominated by a thrust fault. The slips are concentrated in a depth of 5–7 km with a maximum slip of 0.29 m. The estimated total seismic moment is 1.688×10^{18} Nm, corresponding to a magnitude of M_w 6.1. The seismogenic fault is the Kalping fault which has a listric structure. The coseismic deformation only occurred on the décollement layer and did not involve the ramp segment. The coseismic Coulomb stress changes have enhanced the stress on the deep margin of the Jiashi earthquake rupture area, indicating that there is still the possibility of strong earthquakes in this region in the future.

Keywords: Jiashi earthquake, InSAR, Coseismic deformation, Source model, Coulomb stress

Introduction

An M_w 6.0 earthquake struck Jiashi (39.83° N, 77.21° E) in Xinjiang, western China on January 19, 2020 (Fig. 1a). The focal mechanism solutions from the United States Geological Survey (USGS) and Global Centroid Moment Tensor (GCMT) indicated that the Jiashi earthquake was caused by a thrust fault with a slight strike-slip (Table 1).

The epicenter of the Jiashi earthquake is located at the southern margin of the Kalpingtag thrust system (Kalping block), which is situated in the basin-mountain junction region between the south Tian Shan and the

northwestern margin of the Tarim Basin. The Tian Shan orogen is an intracontinental mountain belt revived from rapid and ongoing convergence in response to the Indo-Eurasian collision. Modern geodetic measurements have been used to study the current characteristics of convergent deformation rates in the Tian Shan area, but the deformation mechanism is still under debate. For example, some researchers suggested that the Tian Shan convergent deformation is formed by concurrent slip across several faults and intermontane basins that span the mountain belt (Abdrakhmatov et al. 1996; Thompson et al. 2002; Zubovich et al. 2010). Most of the convergence is not absorbed by a single predominant fault and the strain field is roughly homogeneous. Other researchers proposed that convergence is not uniformly distributed across the Tian Shan, and the slip on the detachment

*Correspondence: qiaoxuejun@gmail.com

² Key Laboratory of Earthquake Geodesy, Institute of Seismology, China Earthquake Administration, Wuhan 430071, China

Full list of author information is available at the end of the article

fault under the Tian Shan dominates the deformation pattern and seismicity of major earthquakes (Yang et al. 2008a, b; Li et al. 2015; Qiao et al. 2017). The existence of large-scale, high slip rate and low-angle detachment fault between the Tian Shan and the foreland basin is the key indicator to distinguish the above two kinematic models. Assuming that there is a main detachment fault, the slip rate and dip angle estimated from geodetic observations are ~ 10 mm/a and $< 5^\circ$, respectively. It is consistent with the speculation of the leading edge thickening model (Yang et al. 2008a, b; Li et al. 2015), but there is still a lack of direct seismic evidence to confirm the existence of such low-angle detachment fault. Therefore, the use of coseismic geodetic measurements to study the slip distribution of strong earthquakes plays an important role in clarifying the geometric structure of active faults in this area.

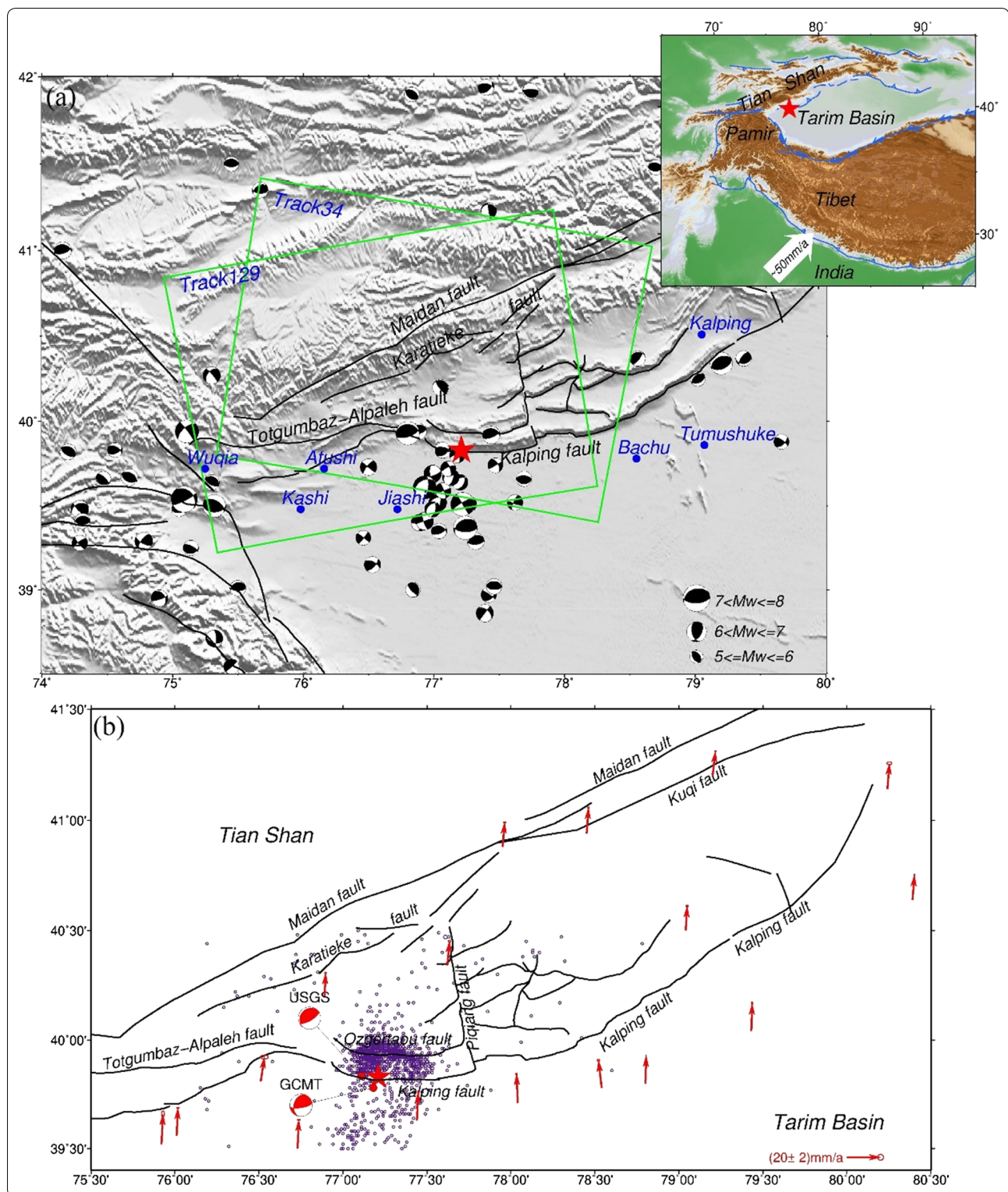
The Tian Shan orogen is resurrected by the far-field effect from the collision between the Indian Plate and the Eurasian plate since the Neogene era. The Kalping block thrusts to the Tarim Basin from the north to the south, forming the Kalpingtag thrust system (Wang, 2007) (Fig. 1b), which is the largest present-day crustal deformation region in the south Tian Shan except the Wuqia–Kashi zone (Avouac et al. 1993). There have been 15 earthquakes over magnitude 6 in the Kalping block just since 1990 such as the 1997 Jiashi strong earthquake swarm. Maidan–Karatieke fault is the northern boundary of the Kalping block, where the Tarim Basin subducts northward to the Tian Shan orogen belt (Allen et al. 1999). It is a large lithosphere-scale fault with obvious vertical movement at the end of the Late Pleistocene. The southern boundary of the Kalping block is the Kalping thrust fault. To the south of the fault is the rigid Tarim Basin with a stable basement. The Kalpingtag thrust system consists of many reverse and anticline fractures from north to south. It is divided into two segments by the Piqiang fault (Fig. 1a). The Jiashi earthquake occurred at the southern margin of the Kalpingtag thrust system, west of the Piqiang fault. The epicenter is between the Kalping fault and Ozgertaou fault (Fig. 1b). Studies from geological and deep seismic-reflection profile indicate

that the geometry of the Kalping fault is a listric-shaped structure (Qu et al. 2003). The dip of the fault is steep at the top and gentle at the bottom. The fault is inclined to the north at an angle with $30\sim 70^\circ$ near the surface. It merges into a detachment surface along the bottom of Cambrian with a depth of about 9 km. The Ozgertaou fault is mostly east–west trending. Its western segment is developed between the Paleogene red sandstone, mudstone and Wuqia group mudstone. Its eastern segment consists of several north inclined thrust faults with a dip of $40\sim 60^\circ$. It roots into the same detachment in the deep just like the Kalping fault (Qu et al. 2003; Yang et al. 2008a, b). The balanced geological cross section revealed that the crustal shortening of the Kalpingtag thrust system on the west side of the Piqiang fault is 45 km. If the initial deformation occurs at the starting time of the Xiyu conglomerate deposition since 2.5 Ma, the crustal shortening rate is 17.3 mm/a (Yang et al. 2008a, b). Modern geodetic measurements have shown that the crustal shortening rate in the Jiashi area relative to the Kazakh block in the northern Tian Shan is about 17–19 mm/a (Wang et al. 2000; Qiao et al. 2000). The characteristics of the Kalping fault and the Ozgertaou fault given by geological investigations is general, which is relatively rough and lack of detailed information such the dip angle with a wide range. Although GPS surveys can provide a fine geometric constraint on the fault, the distribution of stations in the epicenter and adjacent areas is relatively scarce (Fig. 1b). Therefore, the InSAR observations of coseismic deformation are used to highlight the fault geometry and the slip model.

Crustal deformation is the most direct manifestation of an earthquake. Interferometric Synthetic Aperture Radar (InSAR) is a powerful technique, which can quickly obtain large-scale, high-precision, high-resolution surface deformations and has been successfully used for many earthquakes to map the coseismic deformation and study the source model (Wright et al. 2003; Li et al. 2011; Weston et al. 2012; Qiao et al. 2014; Ma et al. 2018; Xiong et al. 2019a, b; Chen et al. 2019). In this study, the coseismic deformation of the 2020 Jiashi earthquake is measured with the InSAR technique using both the ascending and descending interferograms from the Sentinel-1A

(See figure on next page.)

Fig. 1 **a** Distribution map of topography, fault, major historical earthquake and InSAR data in the Jiashi areas. The black beach balls are focal mechanism solutions of the historical earthquake from the GCMT catalog. The red star marks the epicenter of the Jiashi earthquake from CENC. The green box is the coverage of Sentinel SAR data. The blue dots represent the major cities. The black lines are faults that are from the display system of active faults in China provided by the Institute of Geology, China Earthquake Administration. (<http://www.neotectonics.cn/arcgis/apps/webappviewer/index.html?id=3c0d8234c1dc43eaa0bec3ea03bb00bc>). **b** Tectonic map of the Kalping thrust system. The red beach balls are focal mechanism solutions of the Jiashi earthquake from USGS and GCMT. The purple circles represent the aftershocks till 17 June 2020 from CENC. The red arrows represent the horizontal velocity field relative to the Eurasian plate (from CMONOC between 1999 and 2019) provided by the GNSS Data, Products and Services Platform (<http://www.cgps.ac.cn/>) of the China Earthquake Administration



satellite. The fault geometry and slip distribution are retrieved based on coseismic interferograms. Finally, the Coulomb stress changes triggered by this event are

evaluated and the potential seismic hazards are analyzed in the study area.

Table 1 Source parameters for the Jan. 19, 2020 M_w 6.0 Jiashi earthquake

Source	Lat (°)	Lon (°)	Depth (km)	Nodal plane I			Nodal plane II			M_w
				Strike (°)	Dip (°)	Rake (°)	Strike (°)	Dip (°)	Rake (°)	
USGS (W-phase)	39.835	77.11	19.5	221	20	72	60	71	96	6.03
USGS (body wave)	39.835	77.11	4.0	262	9	105	67	81	88	6.05
GCMT	39.78	77.18	12	196	37	30	81	72	123	6.0
GFZ	39.80	77.10	10	222	16	77	56	75	94	6.1
InSAR (a*)	39.91	77.30	6.30	274.8	8.8	110.8 (d*)	–	–	–	6.1
	±0.1 km	±0.1 km	±0.1	±0.1	±0.3					
InSAR (b*)	39.90	77.30	4.15	274.8	52 (c*)	110.7 (d*)	–	–	–	6.0

a* represents the planar fault model, b* represents the listric fault model and its dip angle, c* is the dip of the ramp segment, the dip of the flat segment is fixed to be 2°, d* is the mean rake of each patch

InSAR coseismic deformation

The coseismic deformation of the Jiashi earthquake is completely captured and imaged by the Sentinel-1A radar satellite of the Europe Space Agency (ESA). The data are acquired using a very advanced scanning mode called terrain observation with progressive scans (TOPS) in the Interferometric Wide (IW) mode (Table 2), which can effectively reduce the scalloping effect and improve the interference performance. Two pairs of ascending and descending Sentinel-1A images have the shortest temporal interval of 12 days to minimize the effect of afterslip. Meanwhile, the short perpendicular baselines of -57 m and 12 m can reduce the impact of the digital elevation model (DEM) error (Simons et al. 2002).

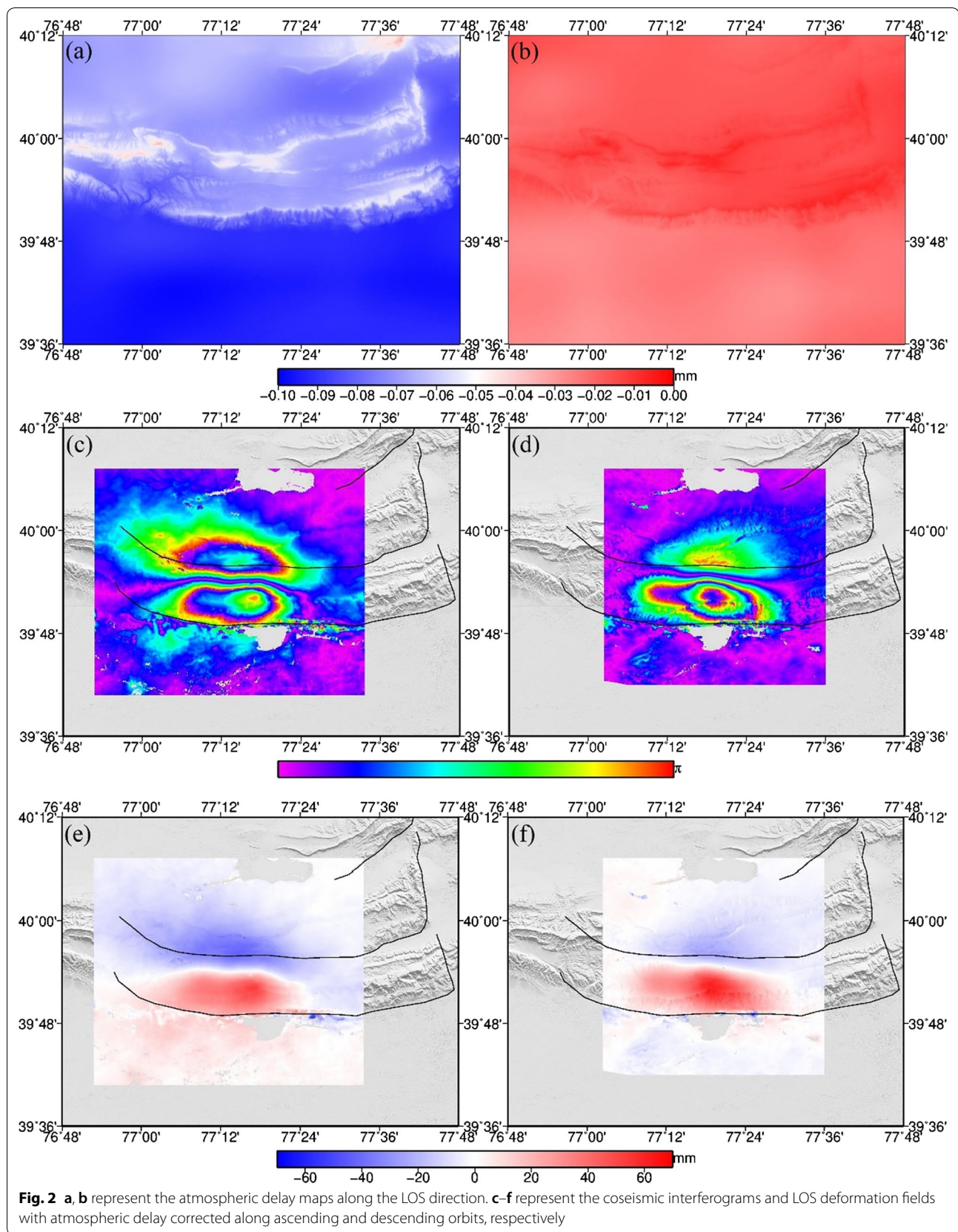
The Sentinel-1A SAR data are processed using the Gamma software (Werner et al. 2000). The interferograms are generated from the Single Look Complex (SLC) products. The multi-look ratio between the range and azimuth direction is set to 10:2 to improve the signal-to-noise ratio. The accuracy of the azimuth coregistration better than 0.001 pixel is acquired to avoid the phase jumps between subsequent bursts. The Shuttle Radar Topographic Mission (SRTM) DEM with a 30-m spacing resolution is used to remove the phase related to ground topography (Farr and Kobrick 2000). A weighted power spectrum technique is employed to filter the interferograms to reduce the phase noise and achieve a high signal-to-noise ratio result (Goldstein and Werner 1998). The Generic Atmospheric Correction Online Service (GACOS) products for InSAR is

used to correct the atmospheric phase delay (Fig. 2a, 2b) (Yu et al. 2018). The minimum cost flow is adopted to unwrap the filtered phase (Pepe and Lanari 2006). Then, the unwrapped interferograms are geocoded to the WGS84 geographic coordinates and converted to displacements along the line of sight (LOS) (Fig. 2).

The coherence of the ascending and descending results is high in most areas because of a high spatial–temporal correlation between images acquired in a Gobi Desert region with little vegetation. The slight discrepancy between the two interferograms can be attributed to different looking incidence and azimuth. The continuous fringes are visible in both ascending and descending interferograms in the epicentral area (Fig. 2c, d). The maximum and minimum LOS displacements are 5.3 cm and -4.2 cm for the T129A interferogram and are 7.2 cm and -3 cm for the T34D interferogram, respectively (Fig. 2e, f). It indicates that the earthquake produced obvious deformation over an area of approximately 40 km by 30 km. The coseismic deformation field is distributed along the Kalping fault and the Ozgertaou fault. The long axis of the deformation field is approximate EW, which is consistent with the strike of the Kalping fault and the Ozgertaou fault. The deformation in the epicentral area between the Kalping fault and the Ozgertaou fault is large and dominated by uplift along LOS. The epicentral area near the Ozgertaou fault and its north side are dominated by subsidence uplift along LOS. The south side of the Kalping fault is deformed slightly. It is uncertain

Table 2 Information of the Sentinel-1 images used for Jiashi earthquake

Flight direction	Track	Primary image date	Secondary image date	Time interval (d)	Perpendicular baseline (m)
Descending	34	2020-01-10	2020-01-22	12	-57
Ascending	129	2020-01-16	2020-01-28	12	12



which fault is the seismogenic fault from InSAR interferogram.

The InSAR coseismic deformation field consists of millions of points and has a high spatial correlation between adjacent observations. It is inefficient to use all of them to invert for the slip model. The LOS coseismic deformation field is firstly masked with a coherence coefficient 0.5 to obtain high-quality deformation data. Then a quadtree algorithm is used to down-sample the data sets to reduce the point number and improve the computational efficiency (Jónsson et al. 2002). Despite the dramatic reduction in quantity, the major features of the original interferograms are well retained in the down-sampled observations (Additional file 1: Figure S1). The unit vector of each point is also calculated from the individual incidence and azimuth angle.

Fault geometry and slip model

A two-step strategy is used to construct the coseismic source model. Firstly, a nonlinear inversion is applied to obtain the optimized fault geometry by assuming a uniform slip on a rectangular fault. Secondly, the distributed slips are estimated by a linear inversion base on a discretized fault plane.

Fault geometry optimization

Based on an elastic and half-space dislocation model, a Multi peak Particle Swarm Optimization (MPSO) algorithm is used to invert for the nine fault parameters consisting of location, length, width, depth, strike, dip, rake and slip by minimizing the misfits between the observed and the model predictions (Feng 2010). The weighted ratio of the ascending and descending datasets is set by 1:1. On the basis of the focal mechanism solutions from different agencies and distribution of after-shocks, we set the strike and dip as 270° and 15° for the initial fault parameters. An optimized plane fault of $22.7 \text{ km} \times 4.7 \text{ km}$ with uniform slip of 0.37 m is derived from MPSO inversion. The strike, dip and rake angle are 274.8° , 8.8° and 105.6° , respectively. The Monte Carlo method is used to estimate the uncertainties of the fault parameters (Table 1, Additional file 1: Figure S2) (Funing et al. 2005). The results show that the inversion is stable and robust. The results indicate that the rupture of this earthquake is dominated by a thrust fault.

Slip model inversion

Based on a variable-slip distribution model, we used the constrained least-squares principle and the Steepest Descent Method (SDM) to invert for rakes and coseismic slips on discretized subfault (Wang et al. 2013). SDM is an iterative optimization algorithm that usually does not require a good initial approximation to achieve

computation converge. The step proportional to negative of the gradient is chosen to achieve the maximum amount of decrease of the objective function at each step.

The dimension of the fault plane is expanded to 50 km along the strike and 20 km along the down-dip direction to avoid edge effects. It is divided into 25×10 subfaults by $2 \text{ km} \times 2 \text{ km}$ for each patch. The position, strike and dip of each subfault are fixed at the optimized values derived from MPSO. We set the rake to a range from 45° to 135° account for the focal mechanisms from GCMT and USGS as well as the result of the nonlinear inversion from MPSO. The depth of the fault top position is 4.58 km. The constrained least squares method is used to solve the following objection function (Wang et al. 2013):

$$F(s) = \|Gs - d\|^2 + \alpha^2 \|H\tau\|^2,$$

where G is the Green function relating unit model slip to the predicted displacement, s is the slip on each patch, d is the observed LOS displacement of InSAR, α is the smoothing factor, H is the finite difference approximation of the Laplacian operator, and τ is the shear stress drop. L-curve method is used to determine the optimal smoothing factor, which can balance the roughness of the fault slip and the model misfit (Additional file 1: Figure S3). Finally, the slip model of the Jiashi earthquake is calculated (Fig. 3). The significant slip area is distributed in $8 \sim 42 \text{ km}$ along the strike and $4 \sim 16 \text{ km}$ along the down-dip direction. The maximum slip is 0.29 m and located at 39.91° N , 77.30° E in a depth of 6.30 km beneath the earth's surface (Fig. 3). The total seismic moment estimated from the optimal slip model is $1.688 \times 10^{18} \text{ Nm}$, corresponding to a magnitude of M_w 6.1. The correlation coefficient between the observations and simulations is 95.62%. The Okada dislocation model is used for forward modeling (Okada, 1985). The root-mean-square (RMS) residual between observations and simulations is 5 mm for ascending datasets and 5 mm for descending datasets, respectively (Fig. 4).

Static Coulomb stress changes

The seismogenic fault usually generates considerable static coseismic deformations and cause static coseismic stress changes in the near and far-field after a strong earthquake occurred (Xiong et al. 2019a, b). Computing and analyzing the coseismic Coulomb stress changes is an important means to evaluate the seismic effect on the surrounding faults.

The PSCMP/PSGRN software is used to calculate the coseismic stress changes caused by the Jiashi earthquake (Wang et al. 2006). The effective friction coefficient is set at a common value of 0.4 (King et al. 1994).

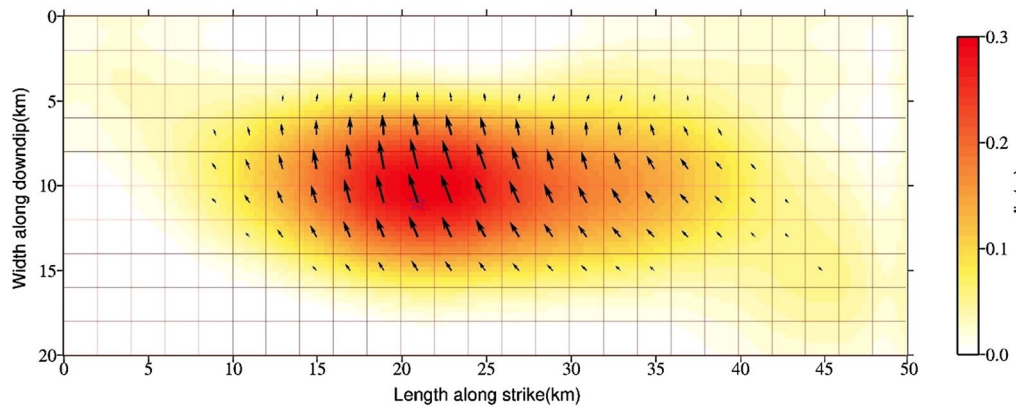


Fig. 3 Coseismic slip model of the Jiashi earthquake

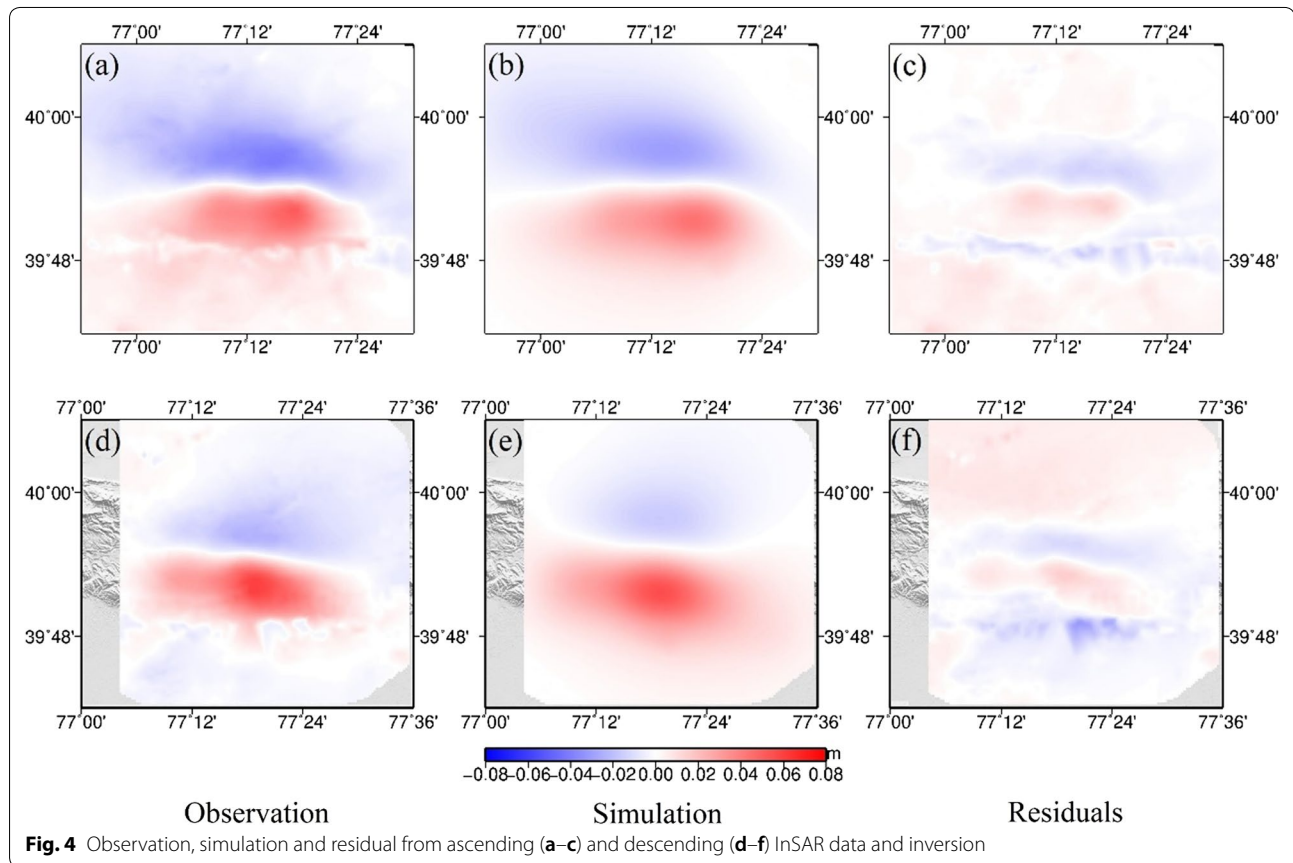


Fig. 4 Observation, simulation and residual from ascending (a–c) and descending (d–f) InSAR data and inversion

The shear modulus is assumed to be 30 GPa. The plane fault inverted above is used as the receiver fault in the calculation of Coulomb stress. The Coulomb stress changes along a profile across the southern edge of the

Kalpingtag nappe show that the area below the rupture of the Jiashi earthquake is a stress-enhancing zone (Fig. 5).

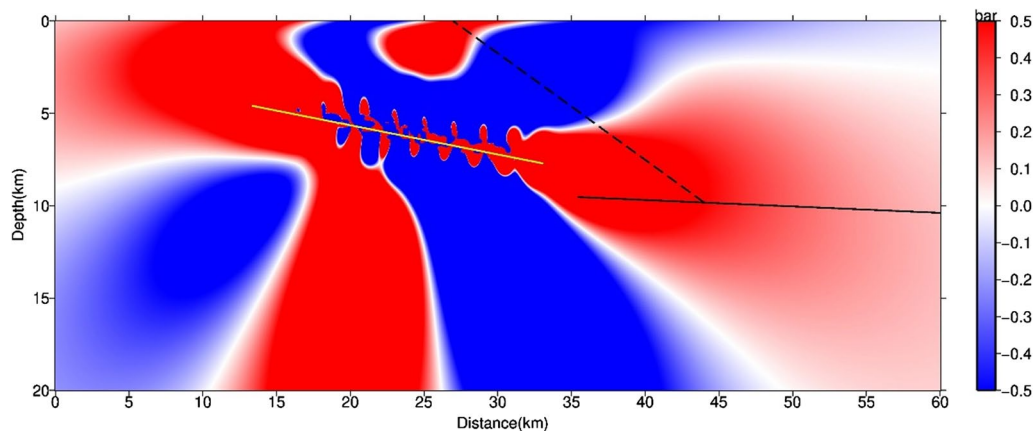


Fig. 5 Coulomb stress change along a profile across the southern margin of the Kalpingtag thrust system. The yellow line represents the planar fault we used. The black line represents the décollement fault. The dashed black line represents the Ozgertaou fault (Zhou, 2013)

Discussion

Planar fault vs. listric fault

The deep seismic-reflection profiles showed that the Kalping fault is a listric structure with flat and ramp segments. The dip of the ramp near the surface is 30–70° (Qu et al. 2003). The dip of the flat segment is 2–3° at a depth of 9 km (Yang et al. 2008a, b; Gao et al. 2013). Therefore, a listric fault geometry is used to invert for the slip model by SDM (Additional file 1: Figure S4). The result showed that the RMS is 7 mm for ascending datasets and 6 mm for descending datasets, respectively. The data-model correlation is 93.45%.

The slip models from the planar fault (Fig. 3) and the listric fault (Additional file 1: Figure S5) both demonstrate that the Jiashi earthquake is a shallow rupture and caused by a thrust fault with slight strike slips. Considering that the planar fault model has the minimum RMS and is more concise, we take the planar fault model as our preferred source model. The Kalping fault is the seismogenic fault, since the position of the modeled fault is close to it.

The preferred model in this study implies the seismogenic fault is very flat with a dip angle 8.8°, which is consistent with the geometrical model of Zhou (2013) who proposed a low-dipping fault of 8.2° for the Kalping thrust system. Studies of geology and seismic reflection profile proposed that the Kalping fault has a listric geometry with typical characteristics of the thin-skinned tectonics (Qu et al. 2003). For thin-skinned tectonics, the sedimentary cover of the thrust sheets is detached from its crystalline basement along a décollement layer. The thickness of the detached cover sediments is typically on the order of 1 to 10 km (Pfiffner, 2017). Here, the coseismic slips of the Jiashi event are distributed in a low dip fault 5–7 km deep underground. The InSAR coseismic

measurements further determined the exact geometry of the listric structure for Kalping fault in this study. It is suggested that the mainshock occurred on the flat segment of the listric fault, while the ramp segment did not rupture.

A shallow event

Results show that the maximum slip of the Jiashi earthquake occurs at the depth 6.3 km which is very shallow. It is contributed to the fault geometry and regional geological settings. The thin-skinned tectonics with shallow décollement structure is the main cause of shallow earthquakes. On the other hand, shallow earthquakes often occur in ancient craton regions, such as the southwest region of Western Australia (Langston 1987; Dawson et al. 2008) and Lake Ontario region in North America (Ma and Atkinson 2006; Kim et al. 2006), where a large number of shallow earthquakes with a depth of less than 5 km occurred. Due to the strong strength of the cold and hard ancient shield, the rock strength in all parts except near the surface exceeds the surrounding deviatoric stress. Driven by deviatoric stress, the fault rupture is difficult to expand to the deep, so it can only rupture at the shallow part to form shallow earthquakes (Langston 1987; Luo et al. 2011). The Tarim Basin, developed on the crystalline basement, has the property of stable craton, which is conducive to form shallow earthquakes in the area.

In orogenic belts, the normal stress due to the large mountain ranges makes the ramp with higher dip angles tend to have greater frictional resistance than the flat with lower dip angles (Styron and Hetland 2015; Yue et al. 2017; Tan et al. 2018). Thus, most earthquakes tend to nucleate on a flat with a lower dip angle, and then expand to a deeper or shallower region (Hubbard et al.

2016). In this context, earthquakes in orogenic belts mostly occur on low-angle detachment faults with a burial depth larger than 10 km, and only a few ruptures of strong earthquakes can expand to ramps near the surface. Therefore, shallow earthquakes larger than M_w 6.0 occurring at the transition zone from fault ramp to fault flat independently in orogenic belts are rare.

Regional seismic risk assessment

Being the front edge of the Kalpingtag thrust system, the slip rate of the Kalping fault is only 1–2 mm/a since late Cenozoic, which is just a quarter of the subduction rate of the Tarim Basin in this region (Yang et al. 2008a, b). It indicates that the deformation pattern of the Kalpingtag thrust system is different from that of other orogenic belts. Deformation of most orogenic belts is dominated by front thrust faults and deep detachment faults, while internal faults within orogenic belts are weakly deformed such as the Himalayan orogeny belt (Stevens and Avouac 2015) and the New Guinea Highlands Fold-and-Thrust Belt (Koulali et al. 2015). However, the Kalping fault and the internal faults of the Kalpingtag nappe have been active since late Quaternary, and the tectonic activities have not completely migrated to the frontal fault of the nappe (Wu et al. 2014). This special deformation pattern makes the faults of Kalpingtag nappe have a low slip rate of 1–3 mm/a, but all faults can accumulate stress and trigger earthquakes. The coseismic Coulomb stress of this earthquake increased the stress of adjacent faults, but the magnitude is not large. For example, the Ozger-taou fault located on the north side of the Kalping fault has a stress disturbance of up to 0.7 bar (Fig. 5).

The faults in the Kalpingtag nappe are locked, accumulating elastic strain, but the detachment fault under the south Tian Shan is free to creep due to the weakening of friction under high-temperature conditions, driving the convergent deformation of the Kalping block (Li et al. 2015). Li et al. (2015) suggested that the locked area of the detachment fault extends to the north of Maidan fault based on the interseismic deformation of InSAR and GPS, while Yang et al. 2008a, b and Qiao et al. (2017) proposed that the locked point of the detachment fault is at the Totgumbaz–Alpaleh fault. The two views are slightly different, but it indicates that the rupture of the Jiashi earthquake is far from the locked point of the detachment fault. The Jiashi earthquake significantly increased the stress in the locked area of the detachment fault (Fig. 5). The maximum stress disturbance is 10.1 bar, which is located at the deep margin of the rupture area. If the remaining locked area of the deep detachment fault is completely ruptured, the deformation width will exceed 50 km, and the released seismic moment is equivalent to an M_w 7.5 earthquake (Wells and Coppersmith 1994).

Conclusion

Based on the coseismic deformation of the 2020 Jiashi M_w 6.0 earthquake obtained from ascending and descending InSAR observations of Sentinel-1A, the fault geometry, slip model and coseismic Coulomb stress changes are calculated.

The source model shows that the Jiashi earthquake occurred on the Kalping fault which is a thrust fault with a listric structure. The main shock only ruptured the flat segment of the listric fault and failed to deform the ramp segment. The coseismic slip is mainly concentrated on a patch of 34 km × 12 km in a depth of 5–7 km. The maximum slip is 0.29 m at a depth of 6.3 km. The released moment is 1.688×10^{18} Nm, corresponding to a magnitude of M_w 6.1.

The coseismic Coulomb stress changes have enhanced the stress on the deep margin of the Jiashi earthquake rupture area, indicating that the seismic risk of this region is increasing. Considering the relatively few after-shocks after the mainshock and strong earthquake swarm records were recorded in Jiashi area, there is still the possibility of another strong earthquake in this region in the future.

Supplementary information

Supplementary information accompanies this paper at <https://doi.org/10.1186/s40623-020-01300-4>.

Additional file 1: Figure S1. (a) and (c) represent observations of ascending and descending data. (b) and (d) represent the down-sampling results of ascending and descending data. **Figure S2.** Uncertainties of the fault parameters computed using the Monte Carlo method. X and Y coordinates are in UTM (zone 43). X, Y, and Depth represent the location of the midpoint of the top boundary of the fault plane. **Figure S3.** Trade-off curve of relative fitting and roughness for the planar fault. **Figure S4.** (a) The geometry of the planar fault and the listric fault. The green line represents the planar fault. The blue line represents the listric fault. The dashed red lines represent the rupture of the Jiashi earthquake on the two faults, respectively. For the listric fault, the dip of the ramp segment is set to 52° determined by a grid search (c). Based on the results of deep seismic-reflection profiles, the dip of the flat segment is set to 2°, and the depth of the top boundaries of the flat segment is set to 9 km. The width of the flat segment is set to 20 km. The elevation difference is magnified 10 times to represent the topography. (b) The surface rupture (the blue line) of the listric fault, which is fixed based on the fault datasets from the Institute of Geology, CEA. Its strike is fixed at 274.8° based on the nonlinear inversion. (c) Distribution of misfit and various top dip angle. (d) Trade-off curve of relative fitting and roughness for the listric fault. **Figure S5.** Coseismic slip model of the Jiashi earthquake with the listric fault. The depth of 9 km is the boundary between the ramp segment and the flat segment.

Abbreviations

InSAR: Interferometric Synthetic Aperture Radar; LOS: Line of sight; CENC: China Earthquake Network Center; USGS: United States Geological Survey; GCMT: Global Centroid Moment Tensor; ESA: Europe Space Agency; TOPS: Terrain observation with progressive scans; IW: Interferometric wide; DEM: Digital elevation model; SLC: Single Look Complex; SRTM: Shuttle Radar Topographic Mission; GACOS: Generic Atmospheric Correction Online Service; RMS: Root-mean-square; CEA: China Earthquake Administration.

Acknowledgements

Appreciate SAR data provided by ESA. SDM program provided by professor Wang Rongjiang is used to invert for the source model. Thanks to Dr. Liu Gang for his helpful advice. Some figures are created by Generic Mapping Tools (Wessel and Smith 1995).

Authors' contributions

PY processed SAR data and analyzed the results; WC provided technical support and useful advice for InSAR processing; WX helped analyze and interpret the results; JL provided the information about the tectonic setting; ZJ contributed to data curation; PY, XQ, WC and JL contributed to funding acquisition; XQ and DW contributed to methodology; ZN contributed to project administration; PY wrote the original draft; XQ and WX revised the manuscript. All authors read and approved the final manuscript.

Funding

This research was funded by the Scientific Research Fund of Institute of Seismology and Institute of Crustal Dynamics, CEA (IS2018126282, IS2018126285), the National Natural Science Foundation of China (41731071, 41874015), and the Spark Program of Earthquake Technology of CEA (XH18054).

Availability of data and materials

The datasets used during the current study are available from the corresponding author on a reasonable request.

Ethics approval and consent to participate

Not applicable.

Consent for publication

Not applicable.

Competing interests

The authors declare that they have no competing interests.

Author details

¹ Institute of Geophysics, China Earthquake Administration, Beijing 100081, China. ² Key Laboratory of Earthquake Geodesy, Institute of Seismology, China Earthquake Administration, Wuhan 430071, China. ³ Earthquake Administration of Xinjiang Uygur Autonomous Region, Urumqi 830011, China.

Received: 25 April 2020 Accepted: 22 October 2020

Published online: 04 November 2020

References

- Abdrakhmatov KY, Aldazhanov SA, Hager BH, Hamburger Mw, Herring TA, Kalabaev KB, Makarov VI, Molnar P, Panasyuk SV, Prilepin MT, Reilinger RE (1996) Relatively recent construction of the Tien Shan inferred from GPS measurements of present-day crustal deformation rates. *Nature* 384(6608):450–453
- Allen MB, Vincent SJ, Wheeler PJ (1999) Late Cenozoic tectonics of the Kalpingtage thrust zone: interactions of the Tien Shan and Tarim Basin, northwest China. *Tectonics* 18(4):639–654
- Avouac JP, Tapponnier P, Bai M, You H, Wang G (1993) Active thrusting and folding along the northern Tien Shan and late Cenozoic rotation of the Tarim relative to Dzungaria and Kazakhstan. *J Geophys Res Solid Earth* 98(B4):6755–6804
- Chen W, Qiao X, Xiong W, Yu P, Nie Z (2019) 2007 Ning'er M_w 6.1 earthquake: a shallow rupture in Southwest China revealed by InSAR measurements. *Earth Space Sci* 6(12):2291–2302. <https://doi.org/10.1029/2019EA000555>
- Dawson J, Cummins P, Tregoning P, Leonard M (2008) Shallow intraplate earthquakes in Western Australia observed by interferometric synthetic aperture radar. *J Geophys Res Solid Earth* 113:B11408. <https://doi.org/10.1029/2008jb005807>
- Farr TG, Kobrick M (2000) Shuttle radar topography Mission produces a wealth of data. *Eos Trans Am Geophys Union* 81(48):583–585. <https://doi.org/10.1029/EO081i048p00583>
- Feng WP, ZH Li (2010) A novel hybrid PSO/Simplex algorithm for determining earthquake source parameters using InSAR data. *Progress Geophys* 25(4):1189–1196. <https://doi.org/10.3969/j.issn.1004-2903.2010.04.007>
- Funning GJ, Parsons B, Wright TJ, Jackson JA, Fielding EJ. (2005). Surface displacements and source parameters of the 2003 Bam (Iran) earthquake from Envisat advanced synthetic aperture radar imagery. *J Geophys Res Solid Earth* 110(B9)
- Gao R, Hou H, Cai X, Knapp JH, He R, Liu J, Xiong X, Guan Y, Li W, Zeng L, Roelcker SW (2013) Fine crustal structure beneath the junction of the southwest Tien Shan and Tarim Basin, NW China. *Lithosphere* 5(4):382–392
- Goldstein RM, Werner CL (1998) Radar interferogram filtering for geophysical applications. *Geophys Res Lett* 25(21):4035–4038. <https://doi.org/10.1029/1998GL900033>
- Hubbard J, Almeida R, Foster A, Sapkota SN, Bürgi P, Tapponnier P (2016) Structural segmentation controlled the 2015 M_w 7.8 Gorkha earthquake rupture in Nepal. *Geology* 44(8):639–642
- Jónsson S, Zebker H, Segall P, Amelung F (2002) Fault slip distribution of the 1999 M_w 7.1 Hector Mine, California, earthquake, estimated from satellite radar and GPS measurements. *Bull Seismol Soc Am* 92(4):1377–1389
- Kim WY, Dineva S, Ma S, Eaton D (2006) The 4 August 2004, Lake Ontario, earthquake. *Seismol Res Lett* 77(1):65–73
- King GC, Stein RS, Lin J (1994) Static stress changes and the triggering of earthquakes. *Bull Seismol Soc Am* 84(3):935–953
- Koulali A, Tregoning P, McClusky S, Stanaway R, Wallace L, Lister G (2015) New Insights into the present-day kinematics of the central and western Papua New Guinea from GPS. *Geophys J Int* 202(2):993–1004
- Langston CA (1987) Depth of faulting during the 1968 Meckering, Australia, earthquake sequence determined from waveform analysis of local seismograms. *J Geophys Res Solid Earth* 92(11):B11561–B11574
- Li Z, Elliott JR, Feng W, Jackson JA, Parsons BE, Walters RJ (2011) The 2010 M_w 6.8 Yushu (Qinghai, China) earthquake: constraints provided by InSAR and body wave seismology. *J Geophys Res Solid Earth* 116:B10302. <https://doi.org/10.1029/2011jb008358>
- Li J, Qiao XJ, Yang SM et al (2015) Detachment fault model characterized for the 3D surface displacement field in the southwestern Tien Shan. *Chinese J Geophys* 058(010):3517–3529. <https://doi.org/10.6038/cjg20151008>
- Luo Y, Ni S, Zeng X et al (2011) The M 5.0 Suining-Tongnan (China) earthquake of 31 January 2010: a destructive earthquake occurring in sedimentary cover. *Chin Sci Bull* 56:57–62. <https://doi.org/10.1007/s11434-010-4276-z>
- Ma S, Atkinson GM (2006) Focal depths for small to moderate earthquakes ($m \geq 2.8$) in Western Quebec, Southern Ontario, and Northern New York. *Bull Seismol Soc Am* 96(2):609–623
- Ma Y, Qiao X, Chen W, Zhou Y (2018) Source model of 2016 M_w 6.6 Aketao earthquake, Xinjiang derived from Sentinel-1 InSAR observation. *Geodesy Geodyn* 9(5):372–377
- Okada Y (1985) Surface deformation due to shear and tensile faults in a half space. *Bull Seismol Soc Am* 75:1135–1154
- Pepe A, Lanari R (2006) On the extension of the minimum cost flow algorithm for phase unwrapping of multitemporal differential SAR interferograms. *IEEE Trans Geosci Remote Sens* 44(9):2374–2383. <https://doi.org/10.1109/TGRS.2006.873207>
- Pfiffner O-A (2017) Thick-skinned and thin-skinned tectonics: a global perspective. *Geosciences* 7(3):1–89. <https://doi.org/10.3390/geosciences7030071>
- Qiao X, Du R, Hua X, Wang X, Wang Q (2000) Monitoring present-day tectonic deformation by GPS in the Northeast Pamir. *Xinjiang. Earthq Res China* 016(4):342–351
- Qiao X, Wang Q, Yang S et al (2014) on the focal mechanism and deformation characteristics for the 2008 M_w 6.7 Wuqia earthquake, Xinjiang by InSAR. *Chin J Geophys* 57(6):1805–1813. <https://doi.org/10.6038/cjg20140612>
- Qiao X, Yu P, Nie Z, Li J, Wang X, Kuzikov SI, Wang Q, Yang S (2017) The crustal deformation revealed by GPS and InSAR in the northwest corner of the Tarim Basin, northwestern China. *Pure Appl Geophys* 174(3):1405–1423
- Qu G, Li Y, Chen J et al (2003) Geometry, kinematics and tectonic evolution of Kalpingtage thrust system. *Earth Sci Front* 010(U08):142–152
- Simons M, Fialko Y, Rivera L (2002) Coseismic deformation from the 1999 M_w 7.1 Hector Mine, California, earthquake as inferred from InSAR and GPS observations. *Bull Seismol Soc Am* 92(4):1390–1402
- Stevens VL, Avouac JP (2015) Interseismic coupling on the main Himalayan thrust. *Geophys Res Lett* 42(14):5828–5837
- Styron RH, Hetland EA (2015) The weight of the mountains: constraints on tectonic stress, friction, and fluid pressure in the 2008 Wenchuan

- earthquake from estimates of topographic loading. *J Geophys Res Solid Earth* 120(4):2697–2716
- Tan X, Yue H, Liu Y, Xu X, Shi F, Xu C, Hao H (2018) Topographic loads modified by fluvial incision impact fault activity in the Longmenshan thrust belt, eastern margin of the Tibetan Plateau. *Tectonics* 37(9):3001–3017
- Thompson SC, Weldon RJ, Rubin CM, Abdrakhmatov K, Molnar P, Berger GW (2002) Late Quaternary slip rates across the central Tien Shan, Kyrgyzstan, central Asia. *J Geophys Res Solid Earth* 107(B9):2203. <https://doi.org/10.1029/2001JB000596>
- Wang Q (2007) Characteristics of Structural deformation and its Controlling Factors of Central and Western Segment in the front of the South Tian Shan. Dissertation, Zhejiang University
- Wang Q, Ding G, Qiao X, Wang X (2000) Research on present crustal deformation in the southern Tianshan (Jiashi), China by GPS geodesy. *Acta Seismol Sin* 3:263–270
- Wang RJ, Lorenzo-Martin F, Roth F (2006) PSGRN/PSCMP—a new code for calculating co- and post-seismic deformation, geoid and gravity changes based on the viscoelastic-gravitational dislocation theory. *Comput Geosci* 32(4):527–541
- Wang R, Diao F, Hoehner A (2013) SDM-A geodetic inversion code incorporating with layered crust structure and curved fault geometry. *EGUGA, EGU2013-2411*
- Wells DL, Coppersmith KJ (1994) New empirical relationships among magnitude, rupture length, rupture width, rupture area, and surface displacement. *Bull Seismol Soc Am* 84(4):974–1002
- Werner C, Wegmüller U, Strozzi T, Wiesmann A (2000) Gamma SAR and interferometric processing software. In: *Proceedings of the ERS ENVISAT Symposium*, Gothenburg, Sweden, 16–20 October 2000
- Wessel P, Smith WHF (1995) New version of the Generic Mapping Tools released. *EOS Trans AGU* 76:329
- Weston J, Ferreira AM, Funning GJ (2012) Systematic comparisons of earthquake source models determined using InSAR and seismic data. *Tectonophysics* 532:61–81
- Wright TJ, Lu Z, Wicks C (2003) Source model for the M_w 6.7, 23 October 2002, Nenana Mountain Earthquake (Alaska) from InSAR. *Geophys Res Lett* 30(18):1974. <https://doi.org/10.1029/2003GL018014>
- Wu C, Alimujiang Dai X, Wu G, Chen J (2014) Discovery of the late-quaternary activity along the eastern segment of maïdan fault in southwest Tianshan and its tectonic implication. *Seismol Geol* 36(4):976–990
- Xiong W, Chen W, Wen Y, Liu G, Nie Z, Qiao X, Xu C (2019a) Insight into the 2017 Mainling M_w 6.5 earthquake: a complicated thrust event beneath the Namche Barwa syntaxis. *Earth Planets Space* 71(1):71
- Xiong W, Chen W, Zhao B, Wen Y, Liu G, Nie Z, Qiao X, Xu C (2019b) Insight into the 2016 Menyuan M_w 5.9 earthquake with InSAR: a blind reverse event promoted by historical earthquakes. *Pure Appl Geophys* 176(2):577–591
- Yang S, Li J, Wang Q (2008a) The deformation pattern and fault rate in the Tianshan Mountains inferred from GPS observations. *Sci China Ser D Earth Sci* 38(7):872–880
- Yang X, Deng Q, Zhang P, Xu X (2008b) Crustal shortening of major nappe structures on the front margins of the Tian Shan. *Seismol Geol* 30(001):11–131
- Yu C, Li Z, Penna NT, Crippa P (2018) Generic atmospheric correction model for Interferometric Synthetic Aperture Radar observations. *J Geophys Res Solid Earth* 123(10):9202–9222
- Yue H, Simons M, Duputel Z, Jiang J, Fielding E, Liang C, Owen S, Moore A, Riel B, Ampuero JP, Samsonov SV (2017) Depth varying rupture properties during the 2015 M_w 7.8 Gorkha (Nepal) earthquake. *Tectonophysics* 714:44–54
- Zhou D (2013) Characteristics of Present-day Crustal Deformation and Seismic Hazard Analysis in the Western and Central Tian Shan. Dissertation, Institute of Geology, China Earthquake Administration
- Zubovich AV, Wang XQ, Scherba YG, Schelochkov GG, Reilinger R, Reigber C, Mosienko OI, Molnar P, Michajljow W, Makarov VI, Li J (2010) GPS velocity field for the Tien Shan and surrounding regions. *Tectonics* 29(6):6014. <https://doi.org/10.1029/2010tc002772>

Publisher's Note

Springer Nature remains neutral with regard to jurisdictional claims in published maps and institutional affiliations.

Submit your manuscript to a SpringerOpen[®] journal and benefit from:

- Convenient online submission
- Rigorous peer review
- Open access: articles freely available online
- High visibility within the field
- Retaining the copyright to your article

Submit your next manuscript at ► [springeropen.com](https://www.springeropen.com)